

Glycine-assisted hydrothermal synthesis of nanostructured $\text{Co}_x\text{Ni}_{1-x}\text{-Al}$ layered triple hydroxides as electrode materials for high-performance supercapacitors

Fang Zhang · Jianwei Jiang · Changzhou Yuan ·
Liang Hao · Laifa Shen · Luojiang Zhang ·
Xiaogang Zhang

Received: 9 July 2011 / Revised: 30 October 2011 / Accepted: 10 November 2011 / Published online: 27 November 2011
© Springer-Verlag 2011

Abstract Nanostructured $\text{Co}_x\text{Ni}_{1-x}\text{-Al}$ layered triple hydroxides ($\text{Co}_x\text{Ni}_{1-x}\text{-Al}$ LTHs) have been successfully synthesized by a facile hydrothermal method using glycine as chelating agent. The samples were characterized by X-ray diffraction, thermogravimetry, Fourier transform infrared spectroscopy and scanning electron microscopy. The morphologies of $\text{Co}_x\text{Ni}_{1-x}\text{-Al}$ LTHs varied with the Co content and its effect on the electrochemical behavior was studied by cyclic voltammetry and galvanostatic charge–discharge techniques. Electrochemical data demonstrated that the $\text{Co}_x\text{Ni}_{1-x}\text{-Al}$ LTHs with Co/Ni molar ratio of 3:2 owned the best performance and delivered a maximum specific capacitance of $1,375 \text{ F g}^{-1}$ at a current density of 0.5 A g^{-1} and a good high-rate capability. The capacitance retained 93.3% of the initial value after 1,000 continuous charge–discharge cycles at a current density of 2 A g^{-1} .

Keywords Layered triple hydroxides · Supercapacitors · Glycine · Nanostructure · Hydrothermal method

Introduction

Electrochemical capacitors (also known as supercapacitors) have drawn increasing attention for energy storage appli-

cations owing to their high power density, high rate capacity, and long cycling life. They show potential applications in hybrid electric vehicles, backup power storage, mobile electric devices, etc. [1–3]. Based on the charge storage mechanism, supercapacitors can be divided into [4]: (1) electrical double-layer capacitors (EDLCs), where the capacitance arises from charge separation at an electrode/electrolyte interface and (2) redox supercapacitors, where the pseudo-capacitance arises from reversible Faradaic reactions occurring at the electrode surface. Pseudocapacitors can store more energy than EDLCs by higher utilization of electrode material. RuO_2 is the best pseudocapacitive material and has specific capacitance as high as 863 F g^{-1} [5]. However, the high cost of Ru limits its commercial applications in electrochemical capacitors. Therefore, it is necessary to develop new electrode materials for replacement of RuO_2 .

Layered double hydroxides (LDHs), also known as anionic clays, are a class of two-dimensional hydroxide-like lamellar materials. The layered structure of the LDHs is constructed by positively charged host layers because of partial substitution of divalent metallic ions with trivalent ones, balanced by interlayer anions and water molecules. LDHs have been used extensively in catalysis [6], ion exchange [7], bio-nanocomposites [8, 9], biosensors [10], and even as substrate for the attachment of Fe_3O_4 nanoparticles [11]. Recently, nickel- and cobalt-based LDHs are explored as electrode materials for supercapacitors due to their layered structure with large interlayer spacing, low cost, and environmental friendliness. For example, Wang et al. prepared the electrode of Ni–Al LDHs grown on the surface of nickel foam by in situ method, which has a specific capacitance of 701 F g^{-1} at a current density of 0.5 A g^{-1} [12]. Malak-Polaczyk et al. [13] prepared Co–Al LDHs/activated carbon composite by a

F. Zhang · J. Jiang · L. Hao · L. Shen · L. Zhang · X. Zhang (✉)
College of Material Science and Engineering,
Nanjing University of Aeronautics and Astronautics,
Nanjing 210016, People's Republic of China
e-mail: azhangxg@163.com

C. Yuan
School of Materials and Engineering,
Anhui University of Technology,
Maanshan 243002, People's Republic of China

simple chemical precipitation method, which exhibited improved electrochemical properties with introducing a small amount of LDHs to activated carbon. Wang et al. [14] found that Co–Al LDHs after annealing at 160 °C have a specific capacitance of 684 F g^{-1} at a current density of 60 mA g^{-1} , which is currently the highest value reported in the case of Co–Al LDHs materials. By using Co–Al LDHs as electrode material instead of Co_3O_4 , the structure can be stabilized by partial isomorphous substitution of Co active sites with Al and the Co utilization ratio can be enhanced over Co_3O_4 [15–17]. As for $\text{Co}_x\text{Ni}_{1-x}$ -Al LTHs, partial cobalt sites are further substituted by Ni. The layered triple hydroxides (LTHs) containing Ni and Co have been proposed as electrode materials with good electrical conductivity, high proton transport, and improved utilization of active sites [18, 19]. A large specific capacitance and long cycling life can be expected for $\text{Co}_x\text{Ni}_{1-x}$ -Al LTHs. Gupta et al. [20] potentiostatically deposited $\text{Co}_x\text{Ni}_{1-x}$ -Al LTHs onto stainless steel and obtained a maximum specific capacitance of $1,263 \text{ F g}^{-1}$.

In this work, we report a simple hydrothermal method to synthesize nanostructured $\text{Co}_x\text{Ni}_{1-x}$ -Al LTHs by using glycine as a chelating agent. The morphologies of the $\text{Co}_x\text{Ni}_{1-x}$ -Al LTHs varied with the Co content. We also investigated the relationships between its chemical composition and electrochemical capacitive behavior in detail. The structure and electrochemical characteristics showed that nanostructured $\text{Co}_x\text{Ni}_{1-x}$ -Al LTHs are a promising supercapacitor electrode material.

Experimental section

Synthesis of $\text{Co}_x\text{Ni}_{1-x}$ -Al LTHs

The experiment was derived from Prevot's work [21], where glycine was used as a chelating agent to synthesize Ni–Al LDHs nanostructures. All chemicals were of AR grade and used without any further purification; deionized water was used in all experiments. Briefly, $\text{Co}_x\text{Ni}_{1-x}$ -Al LTHs were prepared as follows: the (Ni + Co)/Al molar ratio was 2:1; the molar fraction of Co^{2+} in divalent metal cations was 0.0, 0.2, 0.4, 0.6, 0.8, and 1.0, respectively. Stoichiometric Co (NO_3)₂·6H₂O, Ni(NO_3)₂·6H₂O, and Al(NO_3)₃·9H₂O were dissolved in 60 mL deionized water to give solutions with a total metal ion concentration of 0.2 M, and then 0.026 mol glycine and 0.015 mol Na_2SO_4 were introduced to the above solution under vigorous stirring. Then, 10 mL of 5 M NaOH aqueous solution was added all at once with stirring; the pH of the final solution was 13.2. The resulting solution was transferred into an 80-mL Teflon-lined autoclave, which was then sealed and heated in an oven at 100 °C for 24 h. After natural cooling to room temperature, the

product was collected by filtering, washed with deionized water and absolute ethanol several times, and then dried at 60 °C for 12 h. The obtained samples were labeled as $\text{Co}_x\text{Ni}_{1-x}$ -Al LTHs, in which x means the Co content in divalent metal cations.

Characterization

Powder X-ray diffraction (XRD) patterns were recorded on a Bruker D8 Advance instrument using Cu K α radiation ($\lambda = 1.5418 \text{ \AA}$). Thermogravimetric analysis (TGA) experiment was carried out using NETZSCH STA 409 PC, heating was started at $10 \text{ }^\circ\text{C min}^{-1}$ from room temperature to 700 °C in a stream of N_2 (flow, $20 \text{ cm}^3 \text{ min}^{-1}$). Fourier transform infrared (FT-IR) spectra were measured in the range $400\text{--}4,000 \text{ cm}^{-1}$ on a Nicolet 750 spectrophotometer using the KBr pellet technique. Scanning electron microscopy (SEM) analysis of the samples was performed using a LEO-1550 Gemini microscope operating at 5.0 kV accelerating voltage.

Electrochemical tests

The working electrodes were prepared by mixing the electroactive material ($\text{Co}_x\text{Ni}_{1-x}$ -Al LTHs, 80 wt.%), acetylene black (10 wt.%), and poly(tetrafluoro-ethylene) (10 wt.%). The mixture was pressed onto nickel foam (1 cm^2) and dried at 50 °C for 12 h in air. The electrolyte used in this work was 1 M KOH aqueous solution. The electrochemical performance of the $\text{Co}_x\text{Ni}_{1-x}$ -Al LTHs samples was evaluated on a CHI 660 C electrochemical workstation (CH Instruments, Shanghai, China) for cyclic voltammetry (CV) and chronopotentiometry (CP) tests using a three-electrode cell with platinum plate (1 cm^2) as the counter electrode and a saturated calomel electrode as the reference electrode, respectively.

Results and discussions

Structural characterizations

Figure 1 shows the XRD patterns of the $\text{Co}_x\text{Ni}_{1-x}$ -Al LTHs with different Co content x . All the observed peaks including (003), (006), (012), (015), (018), (110), and (113) are typical diffraction patterns of hydroxide-like materials [22, 23], and no other crystalline phases are present. The two strong diffraction peaks appearing at 11.26° and 22.83° , ascribed to (003) and (006) planes, respectively, indicate the growth of crystals in the defined direction. Further analysis of the XRD patterns reveals small differences in the spectrum as a function of the Co content x . With x increasing, the characteristic diffraction peaks slowly narrowed, which can be attributed to the

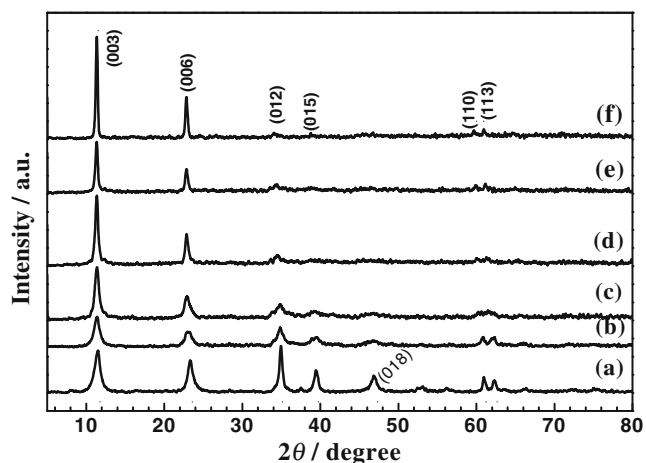


Fig. 1 XRD patterns of the: **a** $\text{Co}_{0.0}\text{Ni}_{1.0}$ -Al LTHs, **b** $\text{Co}_{0.2}\text{Ni}_{0.8}$ -Al LTHs, **c** $\text{Co}_{0.4}\text{Ni}_{0.6}$ -Al LTHs, **d** $\text{Co}_{0.6}\text{Ni}_{0.4}$ -Al LTHs, **e** $\text{Co}_{0.8}\text{Ni}_{0.2}$ -Al LTHs, and **f** $\text{Co}_{1.0}\text{Ni}_{0.0}$ -Al LTHs

substitution of Ni^{2+} by Co^{2+} with a larger ionic radius (Ni^{2+} , 70.0 pm; Co^{2+} , 73.5 pm) [24]. The coherent domain size (thickness of sheet) in the *c* direction could be calculated by the Scherrer equation ($D=0.89\lambda/\beta\cos\theta$) [25], where *D* is the crystalline size, λ is the wavelength of diffraction used ($\lambda=0.15418$ nm), θ is the Bragg diffraction angle, and β is the full width at half-maximum of the (003) reflection. As shown in Table 1, D_{003} increased from 9 nm for the $\text{Co}_{0.0}\text{Ni}_{1.0}$ -Al LTHs sample to 31 nm for the $\text{Co}_{1.0}\text{Ni}_{0.0}$ -Al LTHs sample, implying that the crystallite growth in the *c* direction can be promoted by increasing the Co content.

The thermal behavior of the $\text{Co}_{0.6}\text{Ni}_{0.4}$ -Al LTHs has been studied by TGA technique. As can be seen in Fig. 2, total weight loss of 32 wt.% was obtained throughout the temperature range, which comprises two successive mass losses of 11.6 and 20.4 wt.%. The TG curve shows an initial weight loss in the temperature range from 30 to 200 °C, which is due to the removal of adsorbed water on the outer surface of crystallites and hydrate molecules in the interlayer [26]. Thereafter, the second main weight loss occurs in the temperature range of 200–400 °C, which involves dehydroxylation of the layers and the loss of intercalated anions [27]. The weight loss continued but gradually slowed down after 400 °C.

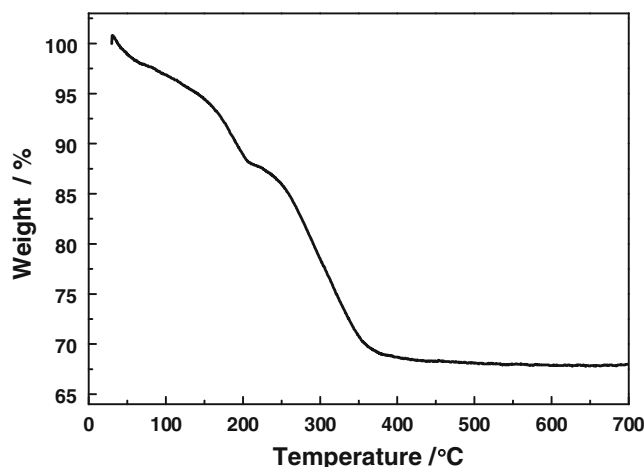


Fig. 2 Thermogravimetric analysis curves of the $\text{Co}_{0.6}\text{Ni}_{0.4}$ -Al LTHs

The FT-IR spectra of the $\text{Co}_x\text{Ni}_{1-x}$ -Al LTHs samples are presented in Fig. 3. These spectra show typical features of LDH materials. The intense and broad band observed around 3,600–3,200 cm^{-1} ascribed to the O–H stretching vibrations arising from metal–hydroxyl groups and interlayer water molecules. The bands appearing at 1,630 cm^{-1} correspond to the bending vibration of water [28]. The band at about 1,384 and 1,364 cm^{-1} are assigned to vibration of NO_3^- and CO_3^{2-} anions [29], respectively. The presence of CO_3^{2-} anion may result from the dissolution of carbon dioxide molecules in water. The band at 1,117 cm^{-1} corresponding to SO_4^{2-} anion is very weak, suggesting a low content of SO_4^{2-} anion. Therefore, it can be concluded that the main anion in the interlayer spaces of $\text{Co}_x\text{Ni}_{1-x}$ -Al LTHs are NO_3^- and CO_3^{2-} . In the low wave number region below 800 cm^{-1} , the adsorptions may be attributed to M–O, O–M–O, and M–O–M (M=Co, Ni, or Al) vibrations [28, 30]. Furthermore, the absorption peaks of the O–H stretching vibrations for six samples (from curves a to f) show a blue shift, which can be attributed to the change in host layer composition.

The SEM images of the $\text{Co}_x\text{Ni}_{1-x}$ -Al LTHs are shown in Fig. 4. As can be seen in Fig. 4a, the $\text{Co}_{0.0}\text{Ni}_{1.0}$ -Al LTH exhibits a honeycomb-like morphology; closer observation of a high-magnification SEM image (inset) shows that such assemblies are built by a large number of curved and intercrossed nanosheets. For the $\text{Co}_{0.2}\text{Ni}_{0.8}$ -Al

Table 1 Crystal parameters of $\text{Co}_x\text{Ni}_{1-x}$ -Al LTHs with varying *x*

<i>x</i>	d_{003}/nm	d_{006}/nm	c^a/nm	d_{110}/nm	a^b/nm	D_{003}/nm
0.0	0.76885	0.38146	2.29766	0.15191	0.30382	9
0.2	0.77558	0.38341	2.31359	0.15213	0.30426	10
0.4	0.77693	0.38704	2.32652	0.15346	0.30692	13
0.6	0.77830	0.38805	2.33160	0.15379	0.30758	20
0.8	0.77898	0.38904	2.33559	0.15401	0.30802	25
1.0	0.77905	0.38936	2.33665	0.15477	0.30954	31

^a $c=3d_{003}$

^b $a=2d_{110}$

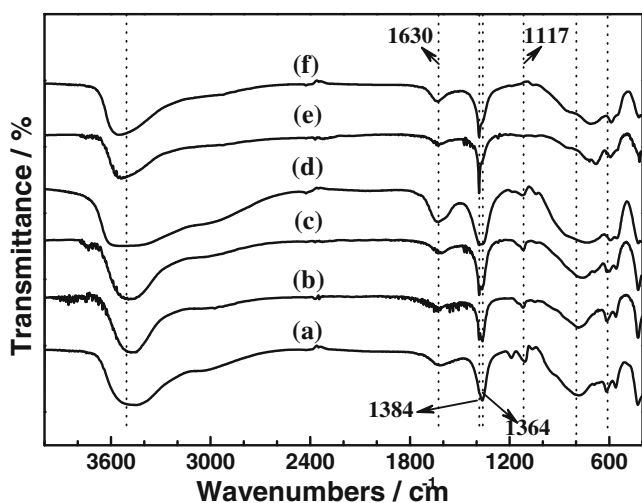
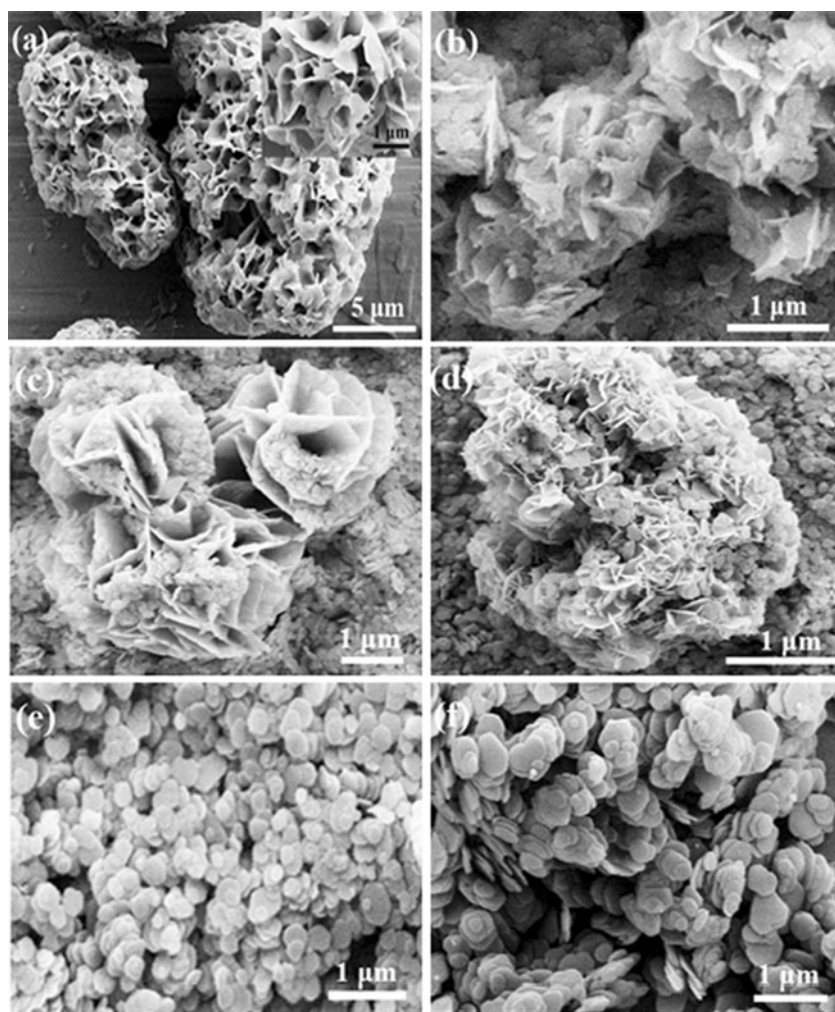


Fig. 3 FT-IR spectra of the $\text{Co}_x\text{Ni}_{1-x}\text{-Al}$ LTHs: **a** $\text{Co}_{0.0}\text{Ni}_{1.0}\text{-Al}$ LTHs, **b** $\text{Co}_{0.2}\text{Ni}_{0.8}\text{-Al}$ LTHs, **c** $\text{Co}_{0.4}\text{Ni}_{0.6}\text{-Al}$ LTHs, **d** $\text{Co}_{0.6}\text{Ni}_{0.4}\text{-Al}$ LTHs, **e** $\text{Co}_{0.8}\text{Ni}_{0.2}\text{-Al}$ LTHs, and **f** $\text{Co}_{1.0}\text{Ni}_{0.0}\text{-Al}$ LTHs

LTHs, a flower-like morphology composed of loose nanosheets was obtained (Fig. 4b). If the Co content x is

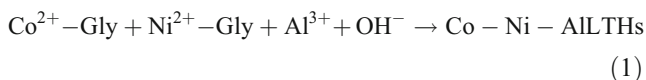
Fig. 4 SEM images of the $\text{Co}_x\text{Ni}_{1-x}\text{-Al}$ LTHs: **a** $\text{Co}_{0.0}\text{Ni}_{1.0}\text{-Al}$ LTHs, **b** $\text{Co}_{0.2}\text{Ni}_{0.8}\text{-Al}$ LTHs, **c** $\text{Co}_{0.4}\text{Ni}_{0.6}\text{-Al}$ LTHs, **d** $\text{Co}_{0.6}\text{Ni}_{0.4}\text{-Al}$ LTHs, **e** $\text{Co}_{0.8}\text{Ni}_{0.2}\text{-Al}$ LTHs, and **f** $\text{Co}_{1.0}\text{Ni}_{0.0}\text{-Al}$ LTHs. The inset image in **a** is a portion of the image at higher magnification



increased to 0.4 and 0.6, as shown in Fig. 4c, d, the LTH nanosheets are assembled into large agglomerates with irregular shape. Upon further increasing x to 0.8, a somewhat hexagonal platelet-like morphology with rounded edges is presented, and the nanoplates become larger and more nanoplates stacked for $\text{Co}_{1.0}\text{Ni}_{0.0}\text{-Al}$ LTHs (Fig. 4f). It can be further found that the morphology of the $\text{Co}_x\text{Ni}_{1-x}\text{-Al}$ LTHs changed from a complicated honeycomb-like morphology to a simple platelet-like structure when x increases.

The generation of complicated structures of the $\text{Co}_x\text{Ni}_{1-x}\text{-Al}$ LTHs ($x < 0.8$) is due to the presence of glycine because the samples prepared under the same experimental conditions without glycine do not give peculiar morphology. It is well known that glycine (Gly, $\text{H}_2\text{N-CH}_2\text{-COOH}$) can coordinate with transition metal ion through carboxylate groups in alkaline medium [31, 32]. The presence of glycine induces the formation of Ni (II) glycinate complex ($\text{Ni}^{2+}\text{-Gly}$) and Co(II) glycinate complex ($\text{Co}^{2+}\text{-Gly}$) at an early stage of the reaction; the complexes are stable at ambient temperature. However, the

complex stabilities decrease with the temperature increasing in the hydrothermal process, which causes the release of Ni²⁺ and Co²⁺ ions. Then, free Ni²⁺ and Co²⁺ in solution precipitate together with Al³⁺ to form Co_xNi_{1-x}-Al LTHs crystal nuclei (Eq. 1). Under the same conditions but in the absence of glycine, metal cations are coprecipitated directly in alkaline solvent. In this synthetic process, LTH nucleation is delayed due to the formation of glycinate complexes which is crucial for high-quality crystal growth [33, 34]. The morphologies of Co_xNi_{1-x}-Al LTHs changed with increasing Co content, which might be due to variation of the nucleation rate. The present method has been adopted to synthesize hierarchical α-Fe₂O₃, and NiO structures [35, 36].



Electrochemical properties

Figure 5a, b shows the CV curves of the Co_xNi_{1-x}-Al LTHs electrodes at the scan rate of 0.5 mV s⁻¹. Very strong redox peaks can be observed in the CV curves for all samples,

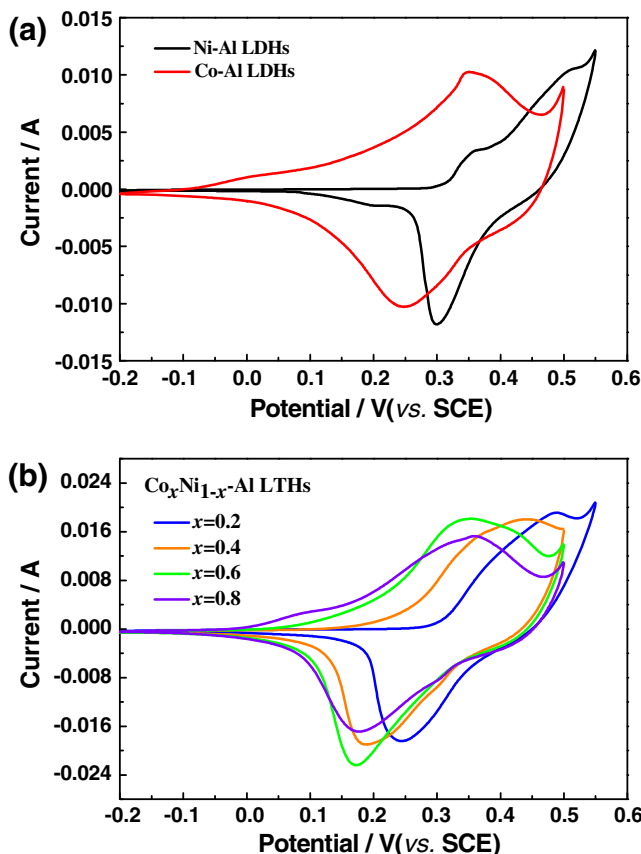
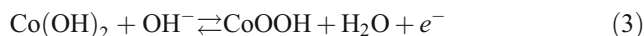
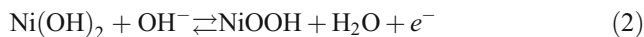


Fig. 5 Cyclic voltammetry curves measured at a scan rate of 0.5 mV s⁻¹

which indicate that Faradic reactions took place; the peak couples correspond to the redox reactions of Ni(OH)₂ and Co(OH)₂ [20, 37]:



There are some changes in the shape of CV curves as the compositions of the Co_xNi_{1-x}-Al LTHs were changed. The anodic and cathodic peaks become broad with increasing the Co content *x*. Furthermore, the oxygen evolution overpotential shifts to a more positive potential as *x* increases, which helps to improve the charge efficiency of the electrode. The potential difference (Δ*E*) between the anodic peak potential (*E*_a) and the cathodic peak potential (*E*_c) is a measure of reversibility in the redox reaction; a smaller value corresponds to better reversibility and vice versa [38]. The Co_{0.6}Ni_{0.4}-Al LTHs have the best reversibility (Δ*E*=172 mV) among the samples. This value is higher than the theoretical value of 59 mV for a reversible one-electron process, which means that the electrode process is quasi-reversible.

Figure 6a, b shows the galvanostatic charge–discharge curves of the Co_xNi_{1-x}-Al LTHs electrodes in 1 M KOH electrolyte at a current density of 1 A g⁻¹ in the potential range of 0–0.5 V. The specific capacitances can be calculated from the discharge curves using the following equation:

$$C_s = \frac{It}{m\Delta V} \quad (5)$$

where *C*_s is the specific capacitance (F g⁻¹), *I* is the charge or discharge current (mA), *t* is the discharging time (s), *m* is the mass of the electroactive material (mg), and Δ*V* is the potential interval of the charge or discharge (V). The discharge curves display two variation ranges, a linear variation of the time dependence of the potential (0–0.2 V), which indicates the double-layer capacitance behavior due to the charge separation between the electrode and electrolyte interface, and a slope variation of the time dependence of the potential (0.2–0.5 V) indicates a typical pseudo-capacitance behavior resulting from the electrochemical redox reaction at the electrode–electrolyte interface [39]. The discharge curves show the pseudo-capacitance characteristic of the Co_xNi_{1-x}-Al LTHs, which is in agreement with CV curves. From Fig. 6a, specific capacitance values of 278 and 657 F g⁻¹ were obtained for Ni–Al LDHs (*x*=0) and Co–Al LDHs (*x*=1), respectively. Because the pseudocapacitance of Co_xNi_{1-x}-Al LTHs is

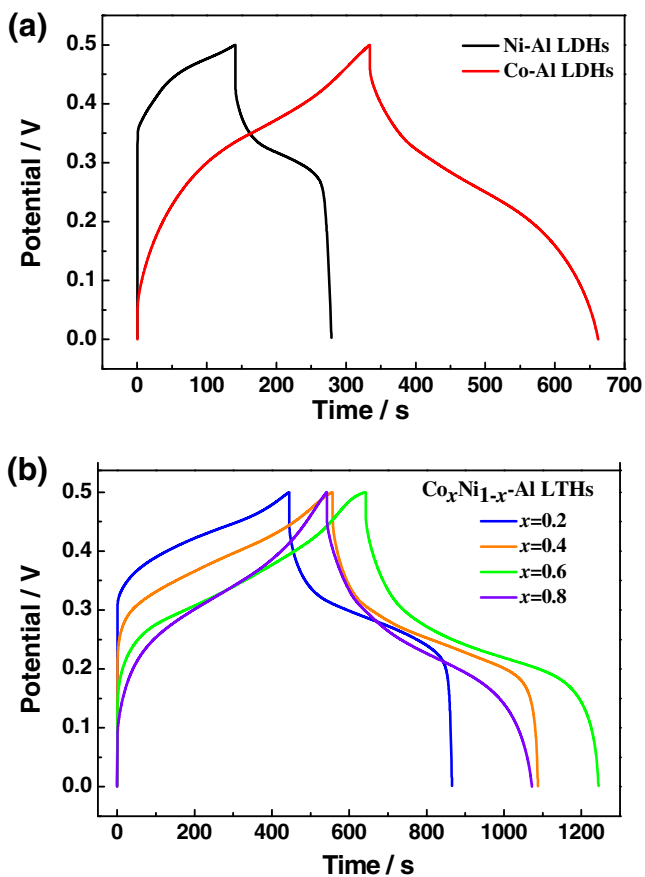


Fig. 6 Galvanostatic charge–discharge curves at 1 A g⁻¹ current density

originated from electroactive Ni and Co sites in the LTHs layers, the specific capacitance of Co_xNi_{1-x}-Al LTHs is dependent on its composition. The relationship between the specific capacitance of the Co_xNi_{1-x}-Al LTHs obtained on the basis of Eq. 5 and the Co content x is plotted in Fig. 7.

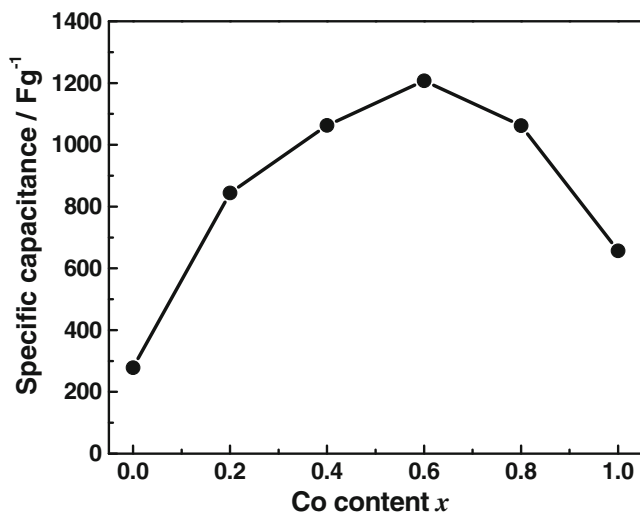


Fig. 7 Relationship between electrode-specific capacitance and the Co content x

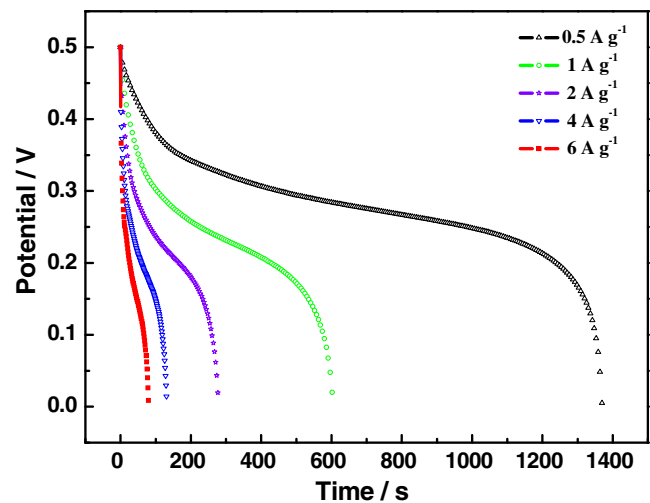


Fig. 8 Discharge curves of the Co_{0.6}Ni_{0.4}-Al LTHs electrode measured at different current densities

The specific capacitance increases as Co content is increased; a maximum specific capacitance of 1,207 Fg⁻¹ was obtained for Co_{0.6}Ni_{0.4}-Al LTHs. As the Co content increases beyond 0.6, the specific capacitance decreases to 1,062 Fg⁻¹ for Co_{0.8}Ni_{0.2}-Al LTHs. These results are in good agreement with Liu's results. [18] The improved electrochemical characteristics can be attributed to the synergistic effects of coprecipitated Ni and Co species. Firstly, cobalt doping is generally considered to significantly improve the performance of Ni(OH)₂ through affecting both the ionic and the electric conductivity of the active material [40–45]. Co(II) was oxidized to CoOOH during charge and might maintain good conductivity, which acts as a current pathway and increases the electron conductivity. Because cobalt is homogeneously distributed in the LTHs slab and thus the conductivity of Co_xNi_{1-x}-Al LTHs is maximized, the active material can be fully used in the

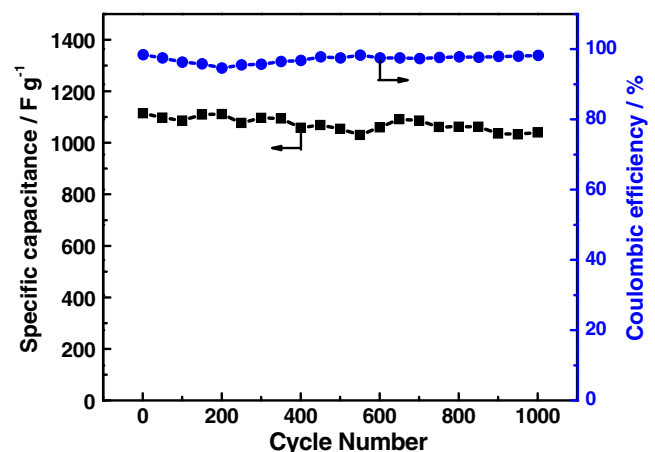


Fig. 9 Cycling stability of the Co_{0.6}Ni_{0.4}-Al LTHs electrode at a current density of 2 A g⁻¹

charge–discharge process. Secondly, the introduction of cobalt increases the oxygen overpotential and improves electrochemical reversibility (see Fig. 5), which is beneficial in maintaining charging efficiency and promoting the utilization of the $\text{Co}_x\text{Ni}_{1-x}\text{-Al}$ LTHs active material. [46] Thirdly, it is indicated that the pseudocapacitance, originating from faradaic redox reactions, is relative to proton transfer. [29] Ni–Al LDHs doped with Co can facilitate the intercalation of protons with the increase of interlayer spacing (see Table 1). [47]

To further quantify the rate performance of the $\text{Co}_{0.6}\text{Ni}_{0.4}\text{-Al}$ LTHs electrode, CP measurements were carried out at different current densities, and the discharge curves are shown in Fig. 8. The calculated specific capacitance values are found to be 1,375, 1,207, 1,116, 1,054, and 962 F g^{-1} at the current density of 0.5, 1, 2, 4, and 6 A g^{-1} , respectively. The $\text{Co}_{0.6}\text{Ni}_{0.4}\text{-Al}$ LTHs electrode preserves about 70% capacitance retention even at a current density of 6 A g^{-1} , indicating its good rate performance. For practical application of an electrochemical capacitor, cycling stability is very important. Figure 9 displays the specific capacitance and coulombic efficiency of the $\text{Co}_{0.6}\text{Ni}_{0.4}\text{-Al}$ LTHs electrode as a function of charge–discharge cycle numbers at a current density of 2 A g^{-1} . It can be seen that the specific capacitance decreased to 93.3% of the initial value after 1,000 cycles, indicating that $\text{Co}_{0.6}\text{Ni}_{0.4}\text{-Al}$ electrode has excellent electrochemical stability. In addition, coulombic efficiency is an important parameter for electrochemical capacitors. The coulombic efficiency (η) can be calculated from the galvanostatic charge–discharge curves as in the following equation [48]:

$$\eta = \frac{\Delta t_D}{\Delta t_C} 100\% \quad (6)$$

where Δt_D and Δt_C are the time for galvanostatic discharging and charging, respectively. According to the data shown in Fig. 9, the coulombic efficiency remained high (95–99%) during the cycling process.

Conclusions

In conclusion, nanostructured $\text{Co}_x\text{Ni}_{1-x}\text{-Al}$ LTHs with different Co contents were successfully synthesized by a simple hydrothermal method. XRD and FT-IR spectra have confirmed that $\text{Co}_x\text{Ni}_{1-x}\text{-Al}$ LTHs samples own a hydroxalite-like structure with NO_3^- and CO_3^{2-} as interlayer anions. The obtained $\text{Co}_x\text{Ni}_{1-x}\text{-Al}$ LTHs have porous structure, which facilitates the OH^- ion diffusion during redox reaction. Thus, the $\text{Co}_x\text{Ni}_{1-x}\text{-Al}$ LTHs exhibit excellent electrochemical performance. The results show that the Co content has a significant effect on the specific

capacitance of the $\text{Co}_x\text{Ni}_{1-x}\text{-Al}$ LTHs. The $\text{Co}_{0.6}\text{Ni}_{0.4}\text{-Al}$ LTHs have a maximum specific capacitance of 1,375 F g^{-1} at a current density of 0.5 A g^{-1} , a good high-rate capability and the capacitance loss is only 6.7% after 1,000 cycles.

Acknowledgements The authors gratefully acknowledge the support by National Natural Science Foundation of China (no. 20873064) and Natural Science Foundation of Jiangsu Province (No. BK2011030).

References

- Conway BE (1999) Electrochemical supercapacitors: scientific fundamentals and technological applications. Kluwer Academic, New York
- Bohlen O, Kowal J, Sauer DU (2007) J Power Sources 172:468–475
- Zhang Y, Feng H, Wu XB, Wang LZ, Zhang AQ, Xia TC, Dong HC, Li XF, Zhang LS (2009) Int J Hydrogen Energy 34:4889–4899
- Conway BE (1991) J Electrochem Soc 138:1539–1548
- Jang JH, Machida K, Kim Y, Naoi K (2006) Electrochim Acta 52:1733–1741
- Sels B, Vos DD, Buntinx M, Pierard F, Kirsch-De Mesmaeker A, Jacobs P (1999) Nature 400:855–857
- Liu ZP, Ma RZ, Osada M, Iyi N, Ebina Y, Takada K, Sasaki T (2006) J Am Chem Soc 128:4872–4880
- Darder M, López-Blanco M, Aranda P, Leroux F, Ruiz-Hitzky E (2005) Chem Mater 17:1969–1977
- Leroux F, Gachon J, Besse J-P (2004) J Solid State Chem 177:245–250
- Forano C, Vial S, Mousty C (2006) Curr Nanosci 2:283–294
- Chen CP, Gunawan P, Xu R (2011) J Mater Chem 21:1218
- Wang J, Song YC, Li ZS, Liu Q, Zhou JD, Jing XY, Zhang ML, Jiang ZH (2010) Energy Fuel 24:6463–6467
- Malak-Polaczyk A, Vix-Guterl C, Frackowiak E (2010) Energy Fuel 24:3346–3351
- Wang Y, Yang WS, Zhang SC, Evans DG, Duan X (2005) J Electrochem Soc 152:A2130
- Su LH, Zhang XG, Mi CH, Liu Y (2008) J Power Sources 179:388–394
- Wang Y, Yang WS, Chen C, Evans DG (2008) J Power Sources 184:682–690
- Scavetta E, Ballarin B, Gazzano M, Tonelli D (2009) Electrochim Acta 54:1027–1033
- Liu XM, Zhang YH, Zhang XG, Fu SY (2004) Electrochim Acta 49:3137–3141
- Chen H, Wang JM, Pan T, Zhao YL, Zhang JQ, Cao CN (2003) J Electrochem Soc 150:A1399–A1404
- Gupta V, Gupta S, Miura N (2009) J Power Sources 189:1292–1295
- Prevot V, Caperaa N, Taviot-Gueho C, Forano C (2009) Cryst Growth Des 9:3646–3654
- Arai Y, Ogawa M (2009) Applied Clay Science 42:601–604
- Liang JB, Ma RZ, Iyi N, Ebina Y, Takada K, Sasaki T (2009) Chem Mater 22:371–378
- Shannon RD, Prewitt CT (1969) Acta Crystallogr Sect B 25:925–946
- Zhao Y, Li F, Zhang R, Evans DG, Duan X (2002) Chem Mater 14:4286–4291
- Gerardin C, Kostadinova D, Sanson N, Coq B, Tichit D (2005) Chem Mater 17:6473–6478

27. Wang H, Fan GL, Zheng C, Xiang X, Li F (2010) *Ind Eng Chem Res* 49:2759–2767
28. Villegas JC, Giraldo OH, Laubernds K, Suib SL (2003) *Inorg Chem* 42:5621–5631
29. Hu ZA, Xie YL, Wang YX, Xie LJ, Fu GR, Jin XQ, Zhang ZY, Yang YY, Wu HY (2009) *J Phys Chem C* 113:12502–12508
30. Perez-Ramrez J, Mul G, Kapteijn F, Moulijn JA (2001) *J Mater Chem* 11:821–830
31. Kiss T, Sovago I, Gergely A (1991) *Pure Appl Chem* 63:597–638
32. Casale A, De Robertis A, De Stefano C, Gianguzza A, Patane G, Rigano C, Sammartano S (1995) *Thermochim Acta* 255:109–141
33. Xiao T, Tang YW, Jia ZY, Li DW, Hu XY, Li BH, Luo LJ (2009) *Nanotechnology* 20:475603–475609
34. Zhang DF, Sun LD, Yin JL, Yan CH (2003) *Adv Mater* 15:1022–1025
35. Chen HM, Zhao YQ, Yang MQ, He JH, Chu PK, Zhang J, Wu SH (2010) *Anal Chim Acta* 659:266–273
36. Wang Y, Zhu QS, Zhang HG (2005) *Chem Commun* :5231–5233
37. Gupta V, Gupta S, Miura N (2008) *J Power Sources* 175:680–685
38. Meher SK, Justin P, Rao GR (2010) *Electrochim Acta* 55:8388–8396
39. Zhao DD, Bao SJ, Zhou WJ, Li HL (2007) *Electrochem Commun* 9:869–874
40. Fan Z, Chen JH, Cui KZ, Sun F, Xu Y, Kuang YF (2007) *Electrochim Acta* 52:2959–2965
41. Park JH, Kim S, Park OO, Ko JM (2006) *Appl Phys A* 82:593–597
42. Zheng Z, Huang L, Zhou Y, Hu XW, Ni XM (2009) *Solid State Sci* 11:1439–1443
43. Armstrong RD, Briggs GWD, Charles EA (1988) *J Appl Electrochem* 18:215–219
44. Armstrong RD, Charles EA (1989) *J Power Sources* 25:89–97
45. Chen J, Bradhurst DH, Dou SX, Liu HK (1999) *J Electrochem Soc* 146:3606–3612
46. Hu CC, Cheng CY (2002) *Electrochem Solid-State Lett* 5:A43–A46
47. Zhao YL, Wang JM, Chen H, Pan T, Zhang JQ, Cao CN (2004) *Electrochim Acta* 50:91–98
48. Yuan CZ, Su LH, Gao B, Zhang XG (2008) *Electrochim Acta* 53:7039–7047